LINE-OF-SIGHT EXTRACTION ALGORITHM FOR DEEP-SPACE AUTONOMOUS NAVIGATION

S. A. Bella[*], E. Andreis[†], V. Franzese[‡], P. Panicucci[§], and F. Topputo[¶]

The proliferation of deep-space probes is posing new challenges in navigating them with ground-in-the-loop methods. Ground tracking stations will reach saturation owing to the escalation of small satellites in deep-space. Thus, autonomous guidance, navigation, and control methods that are independent from ground communications are necessary for future deep-space satellites. For deep-space applications, planets are used as beacons to determine the observer state in deep-space using line-of-sight navigation and celestial triangulation. This paper introduces a planets line-of-sight extraction algorithm for deep-space autonomous navigation. In particular, the methodology focuses on image generation, image processing, and line-of-sight extraction. The probe attitude is estimated from generated images and, if a planet is detected, its line-of-sight is extracted to enable the autonomous satellite position estimation. Numerical simualtions show that a 3σ accuracy of 20 arcseconds for the planet line-of-sight can be reached, yielding to a 3σ accuracy of 1000 km for autonomous position estimation during deep-space application.

INTRODUCTION

Miniaturized platforms are gaining more and more interest from space agencies and companies with respect to traditional large satellites. Deep-space missions with miniaturized satellites, such as CubeSats, have been designed or are under study by the major space actors. Examples of miniaturized interplanetary satellites from the European Space Agency (ESA) are M-ARGO (Miniaturized Asteroid Remote Geophysical Observer) [1], LUMIO (Lunar Meteoroid Impacts Observer) [2, 3], and Milani [4]. The National Aeronautics and Space Administration (NASA) is planning several missions exploiting miniaturized platforms after the success of Mars Cube One (MarCO) [5], the first deep-space CubeSat that performed a flyby of Mars.

Spacecraft miniaturization implies a decrease of costs related to the platform. However, the costs due to operating a miniaturized spacecraft in deep-space are similar to large spacecraft as state-of-art radiometric tracking techniques are used [6]. A possible solution to reduce operations costs is to exploit on-board information to perform autonomous navigation without ground support.

Promising autonomous navigation methods exploit observations of planets in the Solar System to understand the probe state. The line-of-sight (LOS) directions to known beacons, i.e. planets, in

[*]Graduate Student, Dept. of Aerospace Science and Technology, Politecnico di Milano, Milano, 20156, Italy.
[†]PhD Candidate, Dept. of Aerospace Science and Technology, Politecnico di Milano, Milano, 20156, Italy.
[‡]Postodoctoral Research Fellow, Dept. of Aerospace Science and Technology, Politecnico di Milano, Milano, 20156, Italy.
[§]Postodoctoral Research Fellow, Dept. of Aerospace Science and Technology, Politecnico di Milano, Milano, 20156, Italy.
[¶]Full Professor, Dept. of Aerospace Science and Technology, Politecnico di Milano, Milano, 20156, Italy.

the Solar System can be used to provide information to estimation schemes and to triangulate the observer's position [7].
This paper tackles the problem of extracting the line-of-sight direction of known Solar System planets to estimate the observer state. Deep-space synthetic images are rendered and processed to extract LOS directions which then provide information to an Extended Kalman Filter (EKF). The spacecraft attitude is estimated from the image as well. The LOS extraction performances, the attitude accuracy, and the navigation accuracy are then characterized for a typical CubeSat mission scenario.
The paper is structured as follows. Section 'Methodology' outlines the image processing to extract the LOS direction and presents the attitude and position estimation methods. Section 'Simulation Environment' describes the simulation environment together with the settings used for the simulations. Section 'Performances' summarizes the performances of the line-of-sight extraction method, the attitude estimation method and the position estimation method. Lastly, concluding remarks are given in Section 'Conclusions'.

METHODOLOGY

Stars and Planets Centroid Computations

When a deep-space image containing planets and stars is taken, their centroids must be computed to enable autonomous spacecraft navigation in terms of position and attitude. This implies the planets and stars centroids detection by following the flowchart in Figure 1.

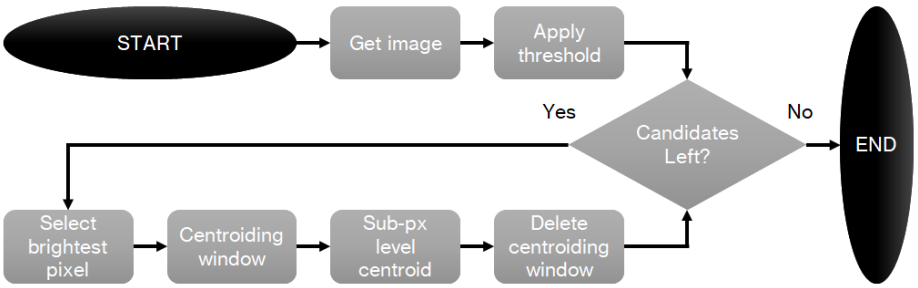

Figure 1: Proposed centroiding algorithm flowchart.

First, the background noise is removed. This can be achieved by setting up a threshold K, expressed in pixel intensity, so that if a pixel intensity $I_{i,j}$ (where i, j denote the pixel coordinates) is lower than the threshold, it is set to zero. Thus:

$$\begin{cases} I_{i,j} = I_{i,j} & \text{if} \quad I_{i,j} > K \\ I_{i,j} = 0 & \text{if} \quad I_{i,j} \leq K \end{cases} \tag{1}$$

The thresholding procedure can be static or dynamic. Static thresholding uses a constant threshold K [8]. Dynamic thresholding uses a constant threshold K which is function of the image intensity [9, 10]. In this work, the following dynamic method is used:

$$\begin{cases} K = \mu + 3\,\sigma \\ \mu = \frac{1}{N} \sum_{i,j} I_{i,j} \\ \sigma = \sqrt{\frac{1}{N} \sum_{i,j} |I_{i,j} - \mu|^2} \end{cases} \tag{2}$$

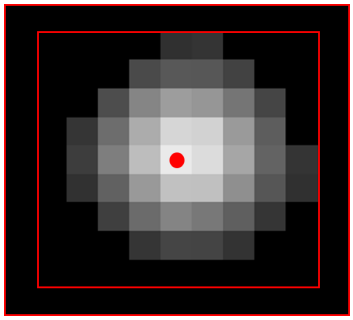

Figure 2: Region of interest (red box) to locate the centroid (red circle).

where N is the total pixels number, μ is the intensity mean, and σ is the intensity standard deviation over the image. Then, the coordinates of the brightest pixels in the image are identified [11]. Second, a squared centroiding window, also known as region of interest (ROI), delimits the object with a margin of one pixel on each side to accurately compute the centroid. An example of this procedure is reported in Figure 2. Then, the computations of the centroid with sub-pixel accuracy is performed by computing the first image moments within each ROI [12]:

$$\begin{cases} I_{00} = \sum_{i,j} I_{i,j}\ w_{i,j} \\ I_{10} = \sum_{i,j} x_i\ I_{i,j}\ w_{i,j} \\ I_{01} = \sum_{i,j} y_j\ I_{i,j}\ w_{i,j} \end{cases} \tag{3}$$

where i and j are the pixels within the ROI, I_{00} is the overall intensity within the ROI, x and y the pixel coordinates, I_{10} and I_{01} are the static moments within the ROI in the two directions, and $w_{i,j}$ is a weighting parameter. In this work, the weighting parameter is defined as $w_{i,j} = I_{i,j}$ to give more importance to brighter pixels. Finally, the sub-pixel centroid coordinates are computed as:

$$x_c = \frac{I_{10}}{I_{00}} \qquad\qquad y_c = \frac{I_{01}}{I_{00}} \tag{4}$$

This process is repeated for all the brightest pixels identified as candidates for stars and planets. This step provides the centroids of the brightest objects in the images which are exploited to determine the spacecraft attitude and to extract the planet LOS.

Star Identification and Attitude Determination

Once the possible candidates for the stars and planets are determined, the spacecraft must identify which are the observed stars and, from this piece of information, it must determine its attitude.
The attitude determination exploits the identification of a geometrical asterism in stars triplets which are matched with a known database. The identification of the Liebe's parameters are used in this work to perform this step [13]. Recall that the minimal number of stars to determine the spacecraft attitude from a star asterism is three.
The Liebe's parameters on a three-star asterism are reported in Figure 3. In the figure, points A, B and C represent the three stars on the celestial sphere and the spherical triangle can be characterized with three parameters owing to its geometrical construction. Therefore, by considering A as a reference star, the geometrical features can be defined as the angular distance from the other stars (e.g., b, c), and the angle between those angular distances (i.e., α). The reference star is selected as

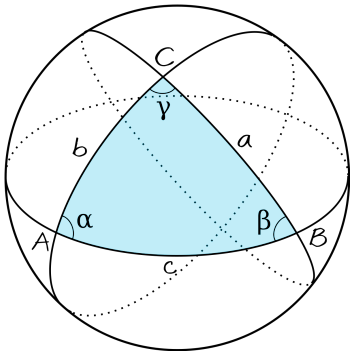

Figure 3: Liebe's parameters a, b, c, α, β, and γ on the spherical triangle formed by A, B, and C.

the brightest of the triplet. Recall that a star brightness is directly linked to the star magnitude which is available from the star catalogue. Note that, as the stars have not been identified yet, the reference star and its magnitude can not be coupled in the catalog. To overcome this problem, an equivalent brightness parameter is defined according to the pixel intensity within the ROI, called I_{ROI}. Thus

$$I_{\text{ROI}} = \sum_{i,j} I_{i,j} \tag{5}$$

This parameter is a coarse estimation of a star brightness, since the photoelectrons coming from the star activate more pixels owing to the sensor defocussing, which is performed to reach sub-pixel accuracy in the centroiding computation. The LOS directions to the points A, B and C are used to estimate the parameters a, b, c, and α exploiting the following equations:

$$\begin{cases} \cos(a) = \hat{\boldsymbol{\rho}}_B^T \, \hat{\boldsymbol{\rho}}_C \\ \cos(b) = \hat{\boldsymbol{\rho}}_A^T \, \hat{\boldsymbol{\rho}}_B \\ \cos(c) = \hat{\boldsymbol{\rho}}_A^T \, \hat{\boldsymbol{\rho}}_C \\ \cos(a) = \cos(b)\cos(c) + \cos(\alpha)\sin(b)\sin(c) \end{cases} \tag{6}$$

The set of Liebe's parameters can then be matched with the database to identify the observed stars. To perform the extraction, the m brightest objects on the image, with brightness defined as in Equation 5, are selected and the Liebe's parameters are computed for all the possible combinations among them. The possible combinations M are given by:

$$M = \left[\frac{m!}{k!(m-k)!} \right] \tag{7}$$

with $k = 3$ as a three-star asterism is chosen. The Liebe's parameters are then stored in a M-by-6 vector for comparison with the database.
The Liebe's parameters of each stars triplet in the M-by-6 vector are compared to the Liebe's parameters in the database according to a cost function J_Δ:

$$J_\Delta = |\Delta\alpha| + |\Delta b| + |\Delta c| \tag{8}$$

where the operator $\Delta(\cdot)$ represents the difference between the Liebe's parameter on the set and on the database.

Finally, the triplet that minimizes J_Δ is selected as the matching one, the stars IDs are extracted from the database and their angular coordinates on the celestial sphere are taken from the Hipparcos catalog. This provides the stars LOS in the inertial reference frame $\mathcal{N}$ are known. Let $\boldsymbol{v}_\mathcal{B}$ and $\boldsymbol{v}_\mathcal{N}$ denote the star LOS in the spacecraft-fixed reference frame $\mathcal{B}$ and in the inertial reference frame $\mathcal{N}$. Let $\boldsymbol{R}_{\mathcal{BN}}$ be the attitude matrix from $\mathcal{B}$ to $\mathcal{N}$, $\boldsymbol{v}_\mathcal{N}$ is computed as:

$$\boldsymbol{v}_\mathcal{N} = \boldsymbol{R}_{\mathcal{BN}} \boldsymbol{v}_\mathcal{B} \tag{9}$$

Once at least three linearly independent directions are known in both the camera and the inertial reference frames, there are a variety of methods that can be applied in order to retrieve the actual attitude matrix. In this work, the singular value decomposition method is applied [14].
According to this method the computation of the attitude matrix $\boldsymbol{R}_{\mathcal{BN}} = \boldsymbol{R}_{\mathcal{NB}}^T$ relies on solving the Wahba's problem:

$$J = \frac{1}{2} \sum_{i=1}^{N} p_i ||\boldsymbol{v}_{\mathcal{B}_i} - \boldsymbol{R}_{\mathcal{NB}} \boldsymbol{v}_{\mathcal{N}_i}||^2 \tag{10}$$

where p_i is a weighting parameter that depends on the ith sensor measurement, and N is the overall number of measurements.
By exploiting the following definitions:

$$\begin{cases} \widetilde{J} = \text{Tr}(\boldsymbol{R}_{\mathcal{NB}} \mathbf{B}^T) \\ \mathbf{B} = \sum_{i=1}^{N} p_i \, \boldsymbol{v}_{\mathcal{B}_i} \boldsymbol{v}_{\mathcal{N}_i}^T \end{cases} \tag{11}$$

and by considering the singular value decomposition $\mathbf{B} = \mathbf{U}\mathbf{S}\mathbf{V}^\intercal$, it has been shown that the Wahba's problem solution is [14]:

$$\boldsymbol{R}_{\mathcal{BN}} = \mathbf{U}\mathbf{M}\mathbf{V}^\intercal; \tag{12}$$

where $\mathbf{M}$ is defined as:

$$\mathbf{M} = \begin{bmatrix} 1 & 0 & 0 \\ 0 & 1 & 0 \\ 0 & 0 & \det(\mathbf{U}) \det(\mathbf{V}) \end{bmatrix} . \tag{13}$$

This procedure provides a way to compute the spacecraft attitude from an image and to enable the LOS extraction and the state estimation.

Line-Of-Sight Extraction and Position Estimation

Once the spacecraft attitude is determined, the planets LOS can be extracted from the image. If no planet is present in the image, a slew maneuver can be performed to point at a Solar System planet. Preferred choice would be to point to the brightest planet, i.e. the one with the lowest magnitude, to ensure an high signal-to-noise ratio in the image. By having an estimation of the spacecraft position and orientation, the the relative geometry and the magnitude *V* can be computed for every planet in the Solar System. This provides the planet to be pointed. Then, the probe computes the pointing direction required to acquire a planet of interest and slews towards that direction to align with it the camera boresight. Then, an image is acquired and processed to detect the planet of interest.
By having a coarse pointing towards the planet and a spacecraft attitude estimation, the acquired image is processed to identify the planet centroiding and to compute the planet LOS. Recall that the stars geometry is known and it can be matched to the stars database, while the planets are

very bright objects in the image which that do not match with any stars asterism. Thus, the planet can be identified accordingly. The centroid coordinates in pixels can be easily converted to LOS information thanks to the pinhole camera model equations. Let $\hat{\boldsymbol{\rho}}^{\mathcal{B}} = [\hat{\rho}_x \ \hat{\rho}_y \ \hat{\rho}_z]^T$ be the planet LOS in the spacecraft-fixed reference frame. From the image coordinates, the planet LOS is computed by exploiting the pinhole camera model:

$$\begin{cases} \rho_z = \frac{f}{\sqrt{x_c^2+y_c^2+f^2}} \\ \rho_x = -x_c \frac{\rho_z}{f} \\ \rho_y = -y_c \frac{\rho_z}{f} \end{cases} \tag{14}$$

where x_c and y_c are the planet centroid in world coordinates, and f is the camera focal length. The LOS is then expressed in the inertial reference frame:

$$\hat{\boldsymbol{\rho}}^{\mathcal{N}} = \boldsymbol{R}_{\mathcal{BN}} \hat{\boldsymbol{\rho}}^{\mathcal{B}} \tag{15}$$

From different planets' LOS in the inertial reference frame, the spacecraft position can be estimated exploiting two observations [15, 16]. Considering Figure 4, the spacecraft position is expressed as:

$$\boldsymbol{r} = \boldsymbol{r}_1 - \rho_1 \, \hat{\boldsymbol{\rho}}_1 = \boldsymbol{r}_2 - \rho_2 \, \hat{\boldsymbol{\rho}}_2 \tag{16}$$

where $\boldsymbol{\rho} = \rho \hat{\boldsymbol{\rho}}$. After multiplying Equation 16 with $\hat{\boldsymbol{\rho}}_1$ and $\hat{\boldsymbol{\rho}}_2$, the system is rewritten as:

$$\underbrace{\begin{bmatrix} -1 & \hat{\boldsymbol{\rho}}_1^T \hat{\boldsymbol{\rho}}_2 \\ -\hat{\boldsymbol{\rho}}_2^T \hat{\boldsymbol{\rho}}_1 & 1 \end{bmatrix}}_{\boldsymbol{A}} \underbrace{\begin{bmatrix} \rho_1 \\ \rho_2 \end{bmatrix}}_{\boldsymbol{x}} = \underbrace{\begin{bmatrix} \hat{\boldsymbol{\rho}}_1^T (\boldsymbol{r}_2 - \boldsymbol{r}_1) \\ \hat{\boldsymbol{\rho}}_2^T (\boldsymbol{r}_2 - \boldsymbol{r}_1) \end{bmatrix}}_{\boldsymbol{b}} \tag{17}$$

This linear system can be solved as $\boldsymbol{x} = \boldsymbol{A}^{-1}\boldsymbol{b}$ to retrieve ρ_1 and ρ_2. Note that the solution is determined only when the matrix $\boldsymbol{A}$ is not singular. This can happen when the two planets are aligned with the observer, i.e. when the angle γ, defined in Figure 4, is equal to 0° or 180°. Then, by exploiting the solution $\boldsymbol{x}$ in Equation 16, the spacecraft inertial position $\boldsymbol{r}$ is retrieved.

By considering that the planets position with respect to the Sun in the inertial reference frame is available from the planets ephemerides, the problem is to compute the planets LOS vectors with respect to the spacecraft positions, $\hat{\boldsymbol{\rho}}_1$ and $\hat{\boldsymbol{\rho}}_2$. To autonomously estimate the spacecraft state on board, an Extended Kalman Filter (EKF) featuring planets LOS aquisition has been developed. Its algorithmic overview is reported in Table 1 for sake of completeness.

The system dynamics is described by the vector field $\boldsymbol{f}$ and process noise $\boldsymbol{w}$. The measurement

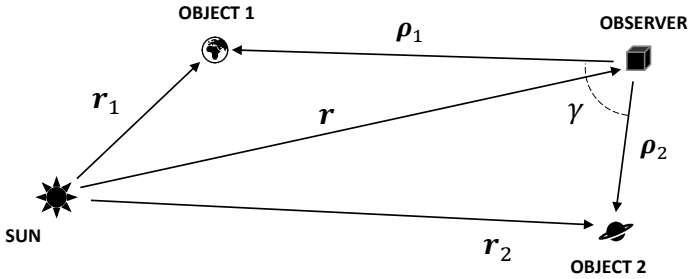

Figure 4: Geometry of the celestial triangulation problem.

Table 1: Scheme of the Extended Kalman Filter

System State Space	$\dot{\boldsymbol{x}} = \boldsymbol{f}(\boldsymbol{x}(t), t) + \boldsymbol{w}$ $\boldsymbol{y}_k = \boldsymbol{h}(\boldsymbol{x}_k) + \boldsymbol{\nu}_k$	
Propagation Block	$\boldsymbol{x}_{p_k} = \boldsymbol{x}_{c_{k-1}} + \int_{t_{k-1}}^{t_k} \boldsymbol{f}(\boldsymbol{x}(t), t)\mathrm{d}t$	$\boldsymbol{x}_{c_0} = E[\boldsymbol{x}_0]$
	$\boldsymbol{\Phi}_k = \boldsymbol{\Phi}_{k-1} + \int_{t_{k-1}}^{t_k} \boldsymbol{F}\boldsymbol{\Phi}\mathrm{d}t$	$\boldsymbol{\Phi}_0 = \boldsymbol{I}$
	$\boldsymbol{S}_k = \boldsymbol{S}_{k-1} + \int_{t_{k-1}}^{t_k} \boldsymbol{\Phi}\boldsymbol{Q}\boldsymbol{\Phi}^T\mathrm{d}t$	$\boldsymbol{S}_0 = \boldsymbol{Q}$
	$\boldsymbol{P}_{p_k} = \boldsymbol{\Phi}_k \boldsymbol{P}_{c_k} \boldsymbol{\Phi}_k^T + \boldsymbol{S}_k$	$\boldsymbol{P}_{c_0} = E[\boldsymbol{x}_0 \boldsymbol{x}_0^T]$
Correction Block	$\boldsymbol{K}_k = \boldsymbol{P}_{p_k}\boldsymbol{H}_k^T(\boldsymbol{H}_k\boldsymbol{P}_{p_k}\boldsymbol{H}_k^T + \boldsymbol{R}_k)^{-1}$	
	$\boldsymbol{x}_{c_k} = \boldsymbol{x}_{p_k} + \boldsymbol{K}_k[\boldsymbol{y}_k - \boldsymbol{h}(\boldsymbol{x}_{p_k})]$	
	$\boldsymbol{P}_{c_k} = (\boldsymbol{I} - \boldsymbol{K}_k\boldsymbol{H}_k)\boldsymbol{P}_{p_k}(\boldsymbol{I} - \boldsymbol{K}_k\boldsymbol{H}_k)^T + \boldsymbol{K}_k\boldsymbol{R}_k\boldsymbol{K}_k^T$	

model is defined by the equation $\boldsymbol{h}$ and white noise $\boldsymbol{\nu}$. In the propagation block at t_k, $\boldsymbol{x}_{p_k}$ is the predicted state vector with error covariance matrix $\boldsymbol{P}_{p_k}$, $\boldsymbol{\Phi}_k$ the state transition matrix (STM), $\boldsymbol{Q}$ the covariance matrix of the process noise, and $\boldsymbol{F}$ the Jacobian matrix of dynamics $\boldsymbol{f}$. In the correction block, $\boldsymbol{K}_k$ represents the Kalman gain, $\boldsymbol{x}_{c_k}$ the corrected state vector with error covariance matrix $\boldsymbol{P}_{c_k}$, $\boldsymbol{R}_k$ the covariance matrix of the measurement noise, $\boldsymbol{H}$ the Jacobian matrix of measurement model $\boldsymbol{h}$, and $\boldsymbol{y}_k$ the observed vector.

SIMULATION ENVIRONMENT

Geometry for Images Generation

In this subsection the needed preliminaries for image rendering are reported in details. The image generation renders two different types of celestial objects, stars and planets, as they are observed from on-board star trackers. Moreover, to correctly generate the image, the object has to be properly located in the image. A star tracker collects the incoming light with an optical sensor, transfers the light to a reading sensor, elaborates the analog information, and extracts the digital data [17]. Thus, it is important to model the geometrical transformations and the sources of errors involved with the representation of the three-dimensional world into an image.

On the one hand, stars are usually stored in stars catalogues, such as the Hipparcos catalogue [18], which provides the right ascension and declination on the stars on the celestial sphere. The first needed step is to understand which are the stars from the catalogue that are observed from the camera. Thus, $\boldsymbol{R}_{\mathcal{BN}}$ is used to perfrom a rotation from the spacecraft-fixed reference frame to the inertial reference frame. This is achieved with a series of counterclockwise rotations taking into account the camera pointing angles, defined as the right ascension $\alpha \in [0°, 360°]$, the declination $\delta \in [-90°, 90°]$, and the twist angle $\phi \in [0°, 360°]$.

By assuming that the camera boresight is coincident with the spacecraft-fixed reference frame third axis, $\boldsymbol{R}_{\mathcal{BN}}$ is given by:

$$\boldsymbol{R}_{\mathcal{BN}} = \boldsymbol{R}_3(\alpha)\, \boldsymbol{R}_2(\pi/2 - \delta)\, \boldsymbol{R}_3(\phi) \tag{18}$$

where $\boldsymbol{R}_k$ denotes the rotation matrix about the axis k. This enable to represent the stars in the spacecraft-fixed reference frame by combining Equations 15 and Equation 18. Recall that, since the stars are inertially-fixed and placed at infinity, their projection in the image plane is not dependent

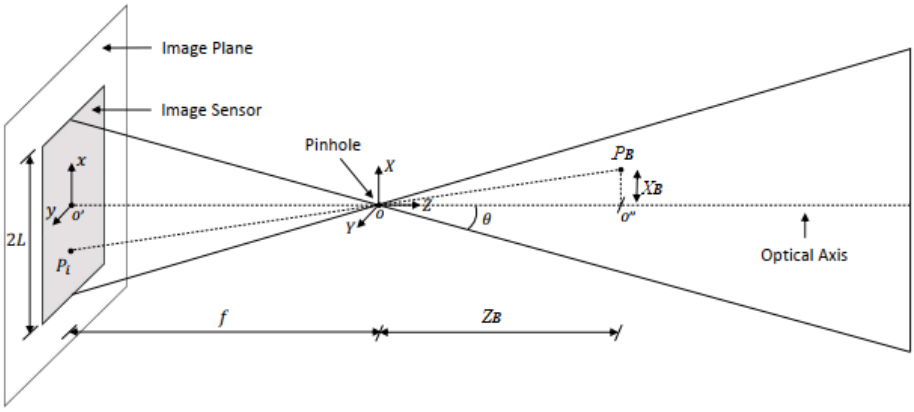

Figure 5: Pinhole camera model [20].

on the spacecraft position in the Solar System. Thus, their inertial positions are extracted from the Hipparcos catalog and used as input to the image generation process [18].
On the one hand, planets position depends on the current epoch. In the current study, only planets smaller than one pixel have been considered because of the high distances in the Solar System. This implies that no raytracing is necessary which simplify the planets rendering procedure. Planets ephemerides are used to retrieve their position $\boldsymbol{r}_{\text{pl}}$ with respect to the Sun in the $\mathcal{N}$ reference frame and, by knowing the spacecraft position $\boldsymbol{r}$ with respect to the Sun, the relative position $\boldsymbol{\rho}$ between a planet and the spacecraft can be computed.
Once the stars and planets positions in the spacecraft-fixed reference frame are computed, they can be projected on the image plane. The projection is performed with the pin-hole camera model [19]. The model parameters are the focal length f, which is the distance between the image plane and the pinhole, the field of view (FOV), which is the observable angle of the real world, and the screen half-size L, which is half-length in world unit of a square-shaped image sensor. These parameters are correlated as follows:

$$\text{FOV} = 2\,\theta = 2\,\arctan\left(\frac{L}{f}\right). \tag{19}$$

In Figure 5 a sketch of the pinhole camera model is shown. Let $P_B = [X_B,\, Y_B,\, Z_B]^T$ be a world point and let $P_i = [x_i,\, y_i]^T$ be its projection onto the image plane. Considering the similarity between the triangles OP_BO" and OP_iO', the projection is given by [16]:

$$\begin{cases} x_i = -f\frac{X_B}{Z_B} \\ y_i = -f\frac{Y_B}{Z_B} \end{cases} \tag{20}$$

Moreover, a screen is composed of a $N_{\text{px}} \times N_{\text{px}}$ matrix of pixels. The image sensor dimension is thus related to the pixels number as:

$$2L = L_{\text{px}}\, N_{\text{px}} \tag{21}$$

This is true when each pixel is squared and has the same characteristic dimension L_{px}.
Finally, the relation to obtain the coordinates in the screen reference frame is expressed in given by:

$$\begin{cases} x_p = -s_x\, x_i + o_x \\ y_p = -s_y\, y_i + o_y \end{cases} \qquad \begin{cases} s_x = s_y = \frac{N_{\text{px}}}{2L} \\ o_x = o_y = \frac{N_{\text{px}}}{2} \end{cases} \tag{22}$$

where the minus sign is due to flipped image, s_x and s_y are the pixel size in world unit, and $[o_x,\ o_y]^T$ is the image center position in the image.

Radiometry for Images Generation

Once the relative geometry and projection between the observer and the sources as stars and planets are defined, it is necessary to derive a radiometric model to consider how the light interacts with the image sensor passing through the camera optics. When gathering light, a certain flux of photons passes through the lens, the photons hit the image sensor generating photoelectrons, and the photoelectrons are collected by the camera electronics. The theoretical approach that supports this model is summarized hereunder [21].
By using the Planck-Einstein relation, a photon energy E_γ can be computed from the speed of light c, the Planck constant h and the wavelength of interest λ as follows:

$$E_\gamma = \frac{c\,h}{\lambda} \tag{23}$$

Then, by knowing the photon flux density F_λ and the bandwidth BW, the photon flux count F_γ can be evaluated:

$$F_\gamma = \frac{F_\lambda\,BW}{E_\gamma} \tag{24}$$

As F_γ is the photon flux count emitted from the object, the photon flux count impacting the image sensor must be computed by considering the optics characteristics. Thus:

$$F_{\gamma/\text{sens}} = F_\gamma\,T_{\text{lens}}\,\pi\left(\frac{d}{2}\right)^2 \tag{25}$$

where T_{lens} is the lens transmission factor, d is the lens aperture, and $F_{\gamma/\text{sens}}$ is the photon count entering the sensor. Then by considering the quantum efficiency Q_e, the electron count on the sensor $F_{e/\text{sens}}$ is gathered:

$$F_{e/\text{sens}} = Q_e\,F_{\gamma/\text{sens}} \tag{26}$$

Finally, the total number of electrons on the sensor $N_{e/\text{sens}}$ depends on the exposure time T as follows:

$$N_{e/\text{sens}} = F_{e/\text{sens}}\,T \tag{27}$$

Note that, thanks to the magnitude definition, it is possible to select a reference object and a reference magnitude V_{ref} to evaluate the others objects' magnitude through similarity:

$$N_{e/\text{sens}}(V) = N_{e/\text{sens}}(V_{\text{ref}}) \times 10^{\frac{(V_{\text{ref}}-V)}{2.5}} \tag{28}$$

On the one hand, stars magnitude is tabulated in the Hipparcos catalogue. On the other hand, planets magnitude must be computed from the planet-spacecraft distance and their phase angle. The apparent magnitude model, based on the intrinsic definition of magnitude, is used for this purpose [22]:

$$V = V(1,0) + 5\,\log_{10}(\|\boldsymbol{\rho}\|^T\,\left\|\boldsymbol{r}_{\text{pl}}\right\|) + m\,, \tag{29}$$

where $V(1,0)$ is the planet absolute magnitude and m is the phase law. Both parameters are reported in Table 2. Note that the phase law depends on the phase angle β defined as the angle between $\boldsymbol{\rho}$ and $\boldsymbol{r}_{\text{pl}}$. As star trackers are generally defocused to increase subpixel accuracy in centroid estimation,

Table 2: Planets magnitude parameters.

	V(1, 0)	m (β in degrees)
Mercury	-0.36	3.8(β/100) - 2.73(β/100)^2 + 2.00(β/100)^3
Venus	-4.29	0.09(β/100) + 2.39(β/100)^2 - 0.65(β/100)^3
Earth [I]	-3.86	0.016β
Mars	-1.52	0.016β
Jupiter	-9.25	0.005β
Saturn	-8.90	0.044β
Uranus	-7.19	0.028β

the photoelectrons spread over many pixels. A normal distribution models this behaviour:

$$N_{e/\text{px}}(x,y) = \frac{N_{e/\text{sens}}(V)}{2\pi\sigma^2} \exp\left(-\left(\frac{(x-x_0)^2 + (y-y_0)^2}{2\sigma^2} \right) \right), \tag{30}$$

where σ represents the object defocus level, and $[x_0, y_0]^T$ are the object center coordinates both expressed in pixel units.
Then, the pixel well capacity Q_{max} is used to saturate pixel with an electron count greater than Q_{max}. Finally the pixel intensity I_{px}, which is an integer number between 0 and 255, is computed as:

$$I_{\text{px}} = 255 \,\text{round}\left(\frac{N_{e/\text{px}}}{Q_{\text{max}}} \right). \tag{31}$$

where round($\cdot$) is the function that rounds each element of the input to its nearest integer, rounding up the singularities (e.g. $0.5 \rightarrow 1$).
Note that there are many noises involved with the image acquisition. For this purpose, a simplified noise model is used to modify the ideal image I_0 before the conversion from photoelectron units to pixel intensity. Each contribution has the following meaning according to its source [23]:

- ε_{Q} is the quantization noise due to A/D conversion;
- ε_{R} is the readout noise due to A/D conversion;
- ε_{FP} is the fixed pattern noise due to the tendency of pixel to be brighter or darker than expected;
- ε_{DS} is dark signal noise due to photoelectrons generated even when no photons are incoming;
- $\varepsilon_{\text{DSNU}}$ is the fixed pattern noise due to dark signal non uniformity;
- $\varepsilon_{\%}$ is a margin that takes into account eventual errors during the estimation of the noise.

Therefore, the noise standard deviation ε is estimated as:

$$\varepsilon = \left[\varepsilon_{\text{Q}} + \varepsilon_{\text{R}} + \varepsilon_{\text{FP}} + \left(\varepsilon_{\text{DS}} + \varepsilon_{\text{DSNU}} \right) T \right] \left(1 + \varepsilon_{\%} \right) \tag{32}$$

[I] Earth phase law is preliminary supposed to be the same as Mars due to lack of data.

Table 3: α-Lyrae optical parameters.

	V [-]	$F_\lambda \left[\frac{\text{W}}{\text{m}^2\,\mu\text{m}}\right]$	λ [nm]
α-Lyrae	0.03	3.44×10^{-8}	555.6

Thanks to this formulation, a noise realization δI_1 is obtained by sampling a Gaussian distribution of zero mean and standard deviation ε. Moreover, the sensor photoresponse non uniformity (PRNU) is model with the constant $\varepsilon_{\text{PRNU}}$. The noise due to the PRNU δI_{PRNU} is computed as follows:

$$\delta I_{\text{PRNU}} = \varepsilon_{\text{PRNU}}\, \mu_I\, \mathbb{1}_{N_{\text{px}}} \tag{33}$$

where μ_I is the image intensity mean over all image pixels and $\mathbb{1}_{N_{\text{px}}}$ is the all-ones matrix of $N_{\text{px}} \times N_{\text{px}}$ size. Finally the noisy image is given by:

$$I = I_0 + \delta I_{\text{PRNU}} + \delta I_1 \tag{34}$$

Images Generation

Once the relative geometry, the projection model and the radiometric model are defined, it is possible to render the synthetic images. Only the stars and planets inside the FOV according to the pointing direction and with the correct magnitude are used for the image generation. A reference celestial object has to be chosen to apply the radiometric equations [21]. The selected object is α–Lyrae, whose properties in terms of magnitude V, flux F_λ and wavelength λ are reported in Table 3. Three different constellations have been used to validate the model. These are the Orion, the Canis Major, and the Crux constellations. The parameters used to simulate the images are reported in Table 4. Note that the noise values applied to simulate the images are also shown in Table 5.
The synthetic images have been validated against real images as shown in Figure 6. The validation process consists in identifying each constellation features in terms of their absolute and relative position. This is due to the fact that the real images are taken on a more complex spectrum than the one simulated. It is possible to notice how the brightest stars are visible, letting the comparison of constellation features possible and thus validating the image generation process.

Simulation Settings

Table 6 shows the characteristics of various optical camera characteristics. These are used as reference to define the optical camera characteristics used for the numerical simulations. The selected camera characteristics are shown in Table 7.
The optical camera characteristics in Table 7 are used to render synthetic images of stars and planets in the Solar System. In particular, the dataset of images considers the spacecraft position randomly picked in a range within 0.5 AU and 10.5 AU from the Sun and pointing directions all around the celestial sphere. The pointing directions are aligned with a set of evenly distributed points on the celestial sphere [25]. The number of points follows the rule

$$N_{\text{pts}}(i_{\text{pts}}, j_{\text{pts}}) = 2 + 10(i_{\text{pts}}^2 + i_{\text{pts}}\, j_{\text{pts}} + j_{\text{pts}}^2) \tag{35}$$

[I] *http://www.sinclairinterplanetary.com/*, last visited on July 2021
[II] *https://www.bluecanyontech.com/*, last visited on July 2021
[III] *https://www.cypress.com/*, last visited on July 2021
[IV] *https://ams.com/*, last visited on July 2021

Table 4: Optical camera setup.

	Orion	Canis Major	Crux
FOV [deg]	17.5	23.5	7.5
f [mm]	25	25	200
T [ms]	300	150	200
N_{px} [px]	1024x1024	1024x1024	1024x1024
F [-]	0.9	0.9	2.5
$Q_e \times T_{lens}$	0.49	0.49	0.49
Q_{max} [e]	14000	14000	14000
σ [px]	2	2	2

Table 5: Noise parameters.

ε_Q [e]	ε_{FP} [e]	ε_{DS} $\left[\frac{e}{s}\right]$	ε_{DSNU} [e]	ε_R [e]	ε_{PRNU} [-]	$\varepsilon_{\%}$ [-]
7	100	200	100	100	0.02	0.2

Table 6: Comparison between different optical cameras characteristics.

	FoV [deg]	Image size [px]	f [mm]	F [-]	$Q_e \times T_{lens}$
NavCam [16]	16×10	2048×1280	40	3.2	-
Sinclair ST-16RT2 [I]	15×20	2592 x 1944	16	1.6	-
Blue Canyon NST [II]	10×12	-	-	-	-
HAS 2 [III]	20×20	1024×1024	-	-	0.45
FaintStar [24]	20×20	1024×1024	-	-	0.49
CMV 4000 [IV]	14×14	2048×2048	44	1.1	0.60

Table 7: Optical camera setup.

FoV [deg]	Image size [px]	f [mm]	F [-]	$Q_e \times T_{lens}$	T [ms]	Q_{max} [e]	σ [px]
20×20	1024×1024	40	3.2	0.49	300	14'000	2

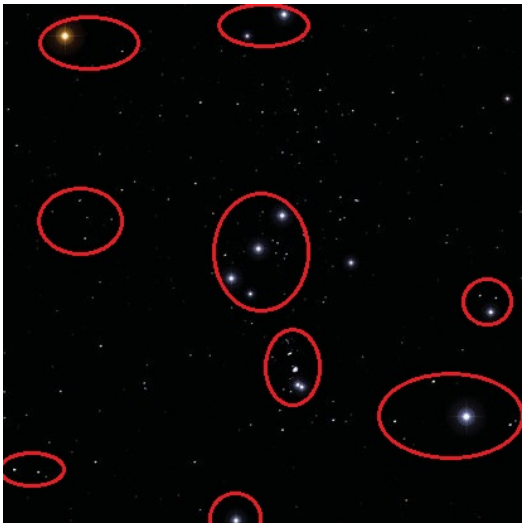

(a) Real image: Orion constellation.

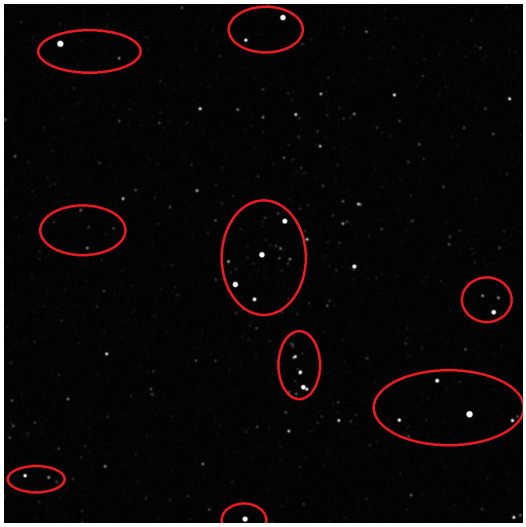

(b) Simulated image: Orion constellation.

(c) Real image: Canis Major constellation.

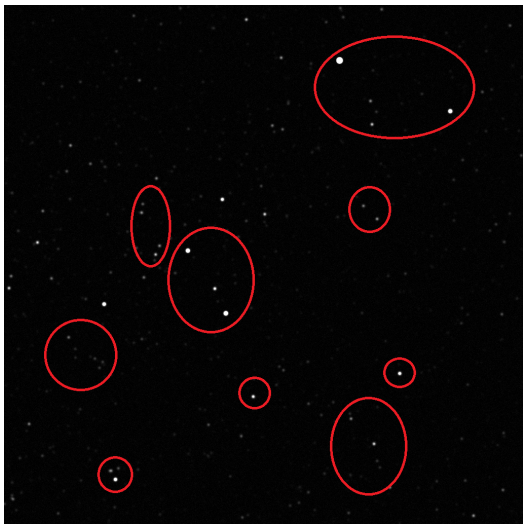

(d) Simulated image: Canis Major constellation.

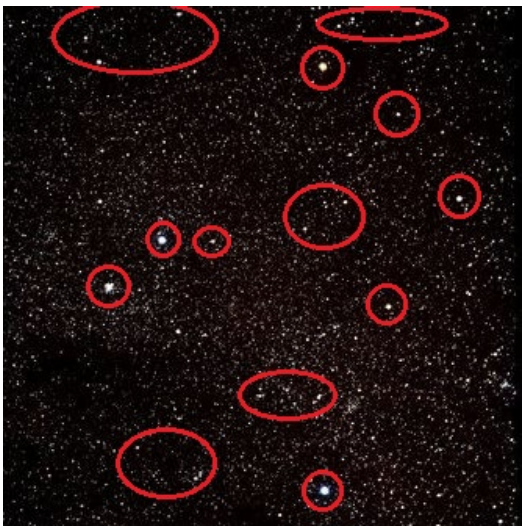

(e) Real image: Crux constellation.

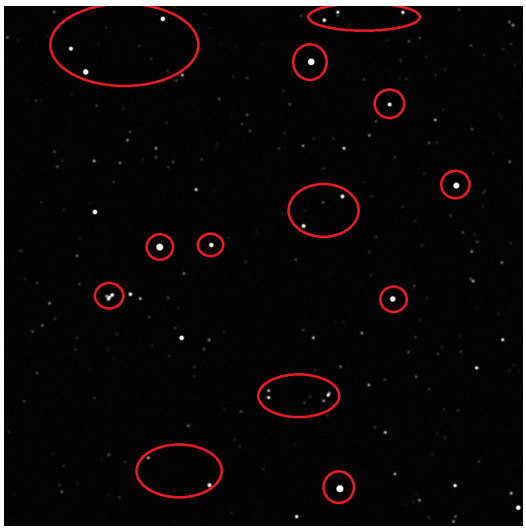

(f) Simulated image: Crux constellation.

Figure 6: Real image versus simulated images for three different constellations.

Table 8: Attitude error as a function of database size M. The first column report the computed attitude determination standard deviation σ_ε. The other columns reports the percentage of sample in the associated bounds.

Database Size M [-]	σ_ε [arcsec]	$\leq \sigma_\varepsilon$ [%]	$\leq 2\sigma_\varepsilon$ [%]	$\leq 3\sigma_\varepsilon$ [%]
936	6.1075	82.39	94.22	98.04
836	6.0558	82.09	93.94	98.04
736	6.2105	83.02	94.03	97.86
636	5.9630	81.99	94.59	97.95
629	6.1015	81.90	94.50	98.23
628	6.0841	81.90	94.59	98.23
627	5.9868	81.62	94.40	98.23
626	5.9444	82.09	94.68	97.95
616	5.5887	81.12	94.58	97.85

which is also known as covering rule, which identifies the number of points to optimally cover a sphere. In this work, $i_{\text{pts}} = j_{\text{pts}} = 6$ which implies $N_{\text{pts}} = 1082$ points over the celestial sphere. In this way, the images dataset is generated to test and characterize both attitude determination and LOS extraction.

PERFORMANCES

Attitude determination

The performances of the attitude determination algorithm are presented in this section. Each image in the images dataset is used to compute the spacecraft attitude and then the attitude determination error statistics are computed. The attitude error ϵ is computed as

$$\epsilon = \arccos(\hat{\boldsymbol{b}}^T \hat{\boldsymbol{b}}_C) \tag{36}$$

where $\hat{\boldsymbol{b}}$ and $\hat{\boldsymbol{b}}_C$ are the true and computed pointing direction, respectively. The attitude determination error is evaluated for each image in the dataset and then a pointing error distribution is gathered. The values of the attitude determination standard deviation σ_ε are reported in Table 8 for different database dimensions M. In the table, the percentage of samples inside the σ_ε, $2\sigma_\varepsilon$ and $3\sigma_\varepsilon$ are reported to show that the distribution is well approximated by a Gaussian distribution.
The numerical simulations show a maximal pointing error of 6.21 arcsec for the attitude determination and it can be noticed that performances start to degrade when the database size M decreases.

Planet acquisition

In this section an example of the planet acquisition procedure is reported to better explain the procedures involved in the overall planet line of sight extraction algorithm. First, the probe tracks some stars to determine its attitude as shown by the red circles in Figure 7a. Then, the probe computes the pointing direction required to acquire a planet of interest and slews towards that direction to align the camera boresight with the planet direction. Then, an image is acquired and processed to detect the planet of interest - red square in Figure 7b. Finally, the planet LOS is obtained by computing the planet centroid, shown in Figure 8, and by exploiting the pinhole camera model.

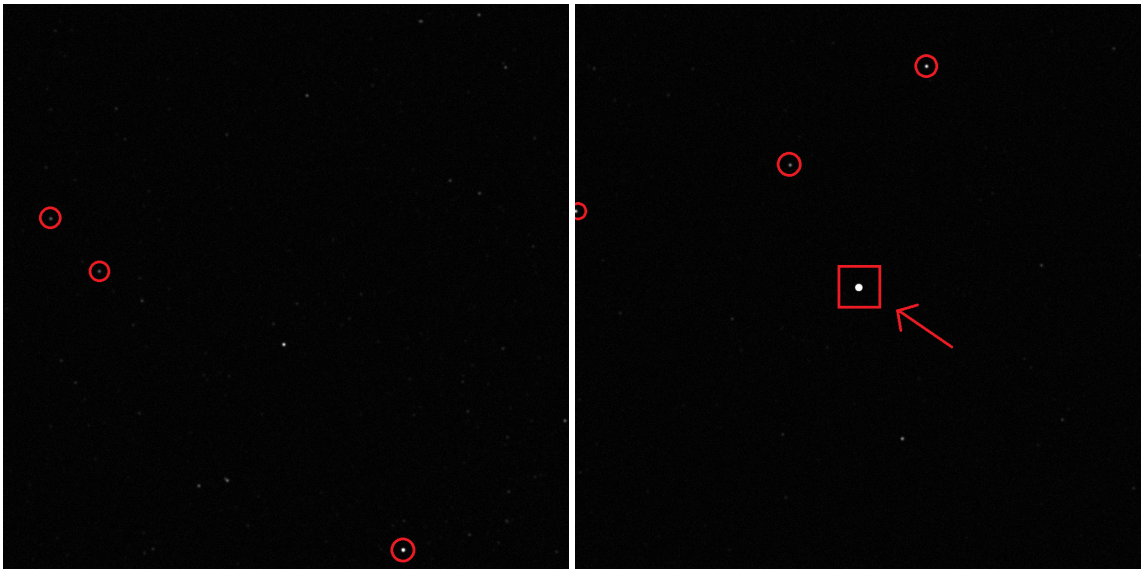

(a) Attitude determination (b) Optimal planet pointing

Figure 7: Example of the planet acquisition procedure

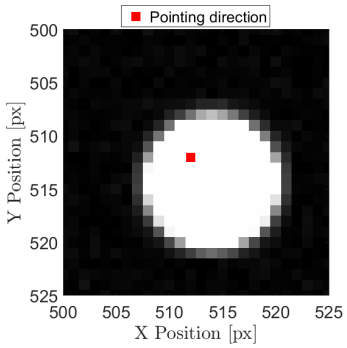

Figure 8: Detail of planet pointing in Figure 7b. The noisy background is visible as well.

Line-of-sight Accuracy

In this section the LOS extraction accuracy is computed to understand the performances of the planet LOS determination for the proposed algorithm. The planet LOS estimation error is computed analogously to the error in the pointing direction given in Equation 36.
To take into account position uncertainties, the each Cartesian component of the nominal position is perturbed with a realization of a white noise with zero mean and standard deviation σ_r. The error on each component is considered uncorrelated to the other Cartesian components. In this work, it is considered a maximal position error of 10^6 km as the observed planets would fall outside the image. Table 9 reports the standard deviation in LOS estimation to the planets. The worst case, which is due to the highest position standard deviation, has a standard deviation $\sigma_{\text{LOS}} = 6.69$ arcseconds, which leads to a $3\sigma_{\text{LOS}}$ LOS accuracy of 20.1 arcseconds for the planets detection. This static characterization of the algorithm is needed and preparatory for the following section where this

standard deviation is used in an EKF to update the spacecraft state. Moreover, in the table, the percentage of samples inside the σ_{LOS}, $2\sigma_{\text{LOS}}$ and $3\sigma_{\text{LOS}}$ are reported to show that the distribution is well approximated by a Gaussian distribution.

Table 9: Line of sight error statistics as a function of position standard deviation σ_r. The first column report the computed attitude determination standard deviation σ_{LOS}. The other columns reports the percentage of sample in the associated bounds.

ε_r [km]	σ_{LOS} [arcsec]	$\leq \sigma_{\text{LOS}}$ [%]	$\leq 2\sigma_{\text{LOS}}$ [%]	$\leq 3\sigma_{\text{LOS}}$ [%]
10^4	6.6924	84.54	88.89	97.96
10^5	5.7415	85.56	91.57	96.67
10^6	5.6085	86.39	91.57	97.22

Position estimation

The position estimation performances in a dynamical simulation are presented in this section. The probe is assumed on an interplanetary transfer toward Mars, during which it estimates its state by measuring the LOS directions to the planets. The LOS is modelled with its nominal value and perturbed with white noise of standard deviation equal to σ_{LOS}. At t_0, the probe nominal position and velocity are $\boldsymbol{r}_0 = [43.9, 145.8, 1.48] \times 10^6$ km and $\boldsymbol{v}_0 = [-29.92, 12.18, 0.43]$ km/s, respectively, and they are initially known with a σ accuracy of 10^6 km and 10^{-1} km/s.
The navigation cycle begins at t_0. The probe tracks a couple of planets one at a time for one hour with a frequency of 0.01 s. Between the two observation windows, a slew maneuver of 20 minutes, where the state is only propagated, is considered. Eventually, the probe state is propagated for 10 days. The entire operational window is composed of 25 navigation legs.
It is assumed that the on-board camera can observe only the planets characterized by relative magnitude lower than 6 and Solar Aspect Angle greater than 35 deg, with a $3\sigma_{\text{LOS}}$ measurement accuracy of 20.1 arcseconds, according to Table 9. Then, the optimal beacons selection strategy [7] is applied to select the best pair of beacons among the visible ones. Figure 9 and Figure 10 show the position and velocity error profiles, respectively. The samples error profile is displayed with blue solid lines, whereas the dashed ones define the 3σ filter covariance bounds. At the end of the operation window, the 3σ error of the probe position and velocity is lower than 480 km and 0.05 m/s.

CONCLUSIONS

This paper shows that autonomous positioning of a deep-space satellite is possible extracting the line-of-sight directions to known planets from optical images. A planet centroid can be detected with an accuracy of 20.1 arcseconds in 3σ confidence after an attitude determination procedure. The error for the whole attitude determination process remains within 18.3 arcseconds in terms of 3σ. By considering these errors in the position estimation method, the spacecraft position can be estimated with an accuracy better than 1000 km in 3σ in deep-space.

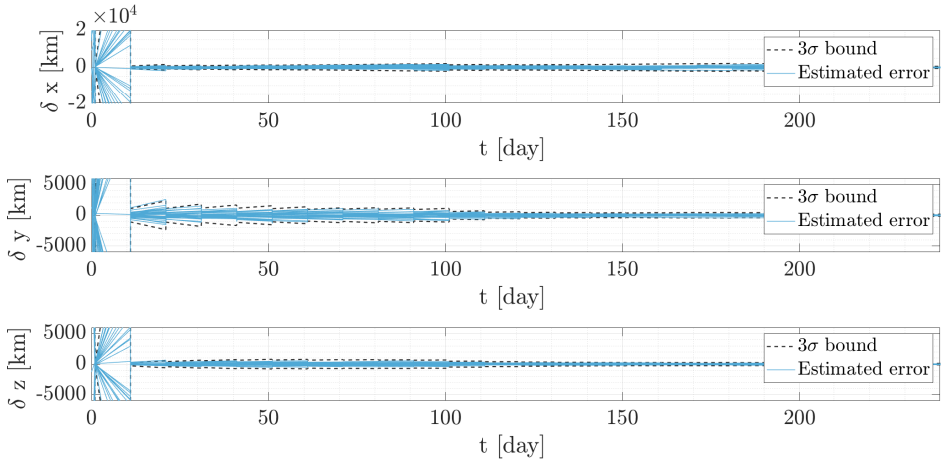

Figure 9: Position error and covariance 3σ bounds. Thirty samples are shown.

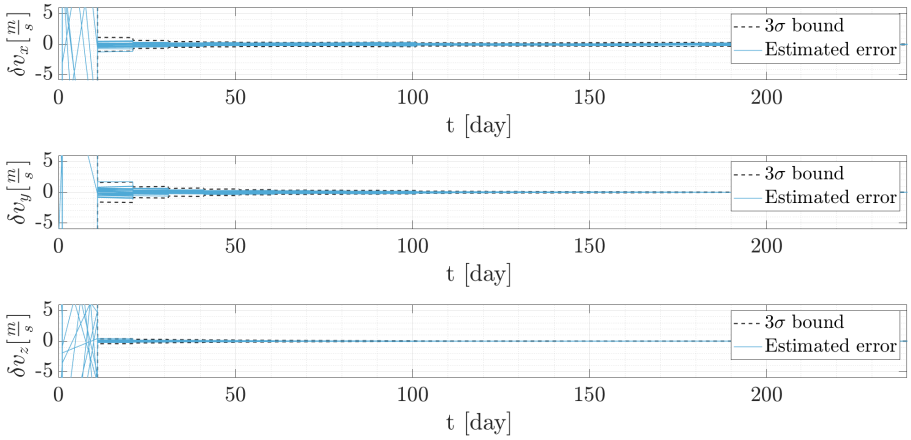

Figure 10: Velocity error and covariance 3σ bounds. Thirty samples are shown.

ACKNOWLEDGMENTS

This research is part of EXTREMA, a project that has received funding from the European Research Council (ERC) under the European Union's Horizon 2020 research and innovation programme (Grant Agreement No. 864697).

REFERENCES

[1] R. Walker, D. Binns, C. Bramanti, M. Casasco, P. Concari, D. Izzo, D. Feili, P. Fernandez, J. G. Fernandez, P. Hager, *et al.*, "Deep-space CubeSats: thinking inside the box," *Astronomy & Geophysics*, Vol. 59, No. 5, 2018, pp. 5–24. DOI: 10.1093/astrogeo/aty237.

[2] F. Topputo, M. Massari, J. Biggs, P. Di Lizia, D. Dei Tos, K. Mani, S. Ceccherini, V. Franzese, A. Cervone, P. Sundaramoorthy, *et al.*, "LUMIO: a cubesat at Earth-Moon L2," *4S Symposium*, 2018, pp. 1–15. Sorrento.

[3] S. Speretta, A. Cervone, P. Sundaramoorthy, R. Noomen, S. Mestry, A. Cipriano, F. Topputo, J. Biggs, P. Di Lizia, M. Massari, K. V. Mani, D. A. Dei Tos, S. Ceccherini, V. Franzese, A. Ivanov, D. Labate, L. Tommasi, A. Jochemsen, J. Gailis, R. Furfaro, V. Reddy, J. Vennekens, and R. Walker, *LUMIO: An*

Autonomous CubeSat for Lunar Exploration, ch. 6, pp. 103–134. Springer International Publishing, 2019. DOI: 10.1007/978-3-030-11536-4_6.

[4] F. Ferrari, V. Franzese, M. Pugliatti, C. Giordano, and F. Topputo, "Preliminary mission profile of Hera's Milani CubeSat," *Advances in Space Research*, Vol. 67, 2021. DOI: 10.1016/j.asr.2020.12.034.

[5] J. Schoolcraft, A. Klesh, and T. Werne, *MarCO: Interplanetary Mission Development on a CubeSat Scale*, pp. 221–231. Springer International Publishing, Space Operations: Contributions from the Global Community, 2017. DOI: 10.1007/978-3-319-51941-8_10.

[6] J. S. B. Catherine L. Thornton, *Radiometric Tracking Techniques for Deep-Space Navigation*. Deep-Space Communications and Navigation Series, Wiley-Interscience, 2003.

[7] V. Franzese and F. Topputo, "Optimal Beacons Selection for Deep-Space Optical Navigation," *The Journal of the Astronautical Sciences*, Vol. 67, 2020, pp. 1775–1792. DOI: 10.1007/s40295-020-00242-z.

[8] J. Jiang, H. Wang, and G. Zhang, "High-Accuracy Synchronous Extraction Algorithm of Star and Celestial Body Features for Optical Navigation Sensor," *IEEE Sensors Journal*, Vol. 18, No. 2, 2018, pp. 713–723, DOI: 10.1109/JSEN.2017.2777493.

[9] L. Kazemi, J. Enright, and T. Dzamba, "Improving star tracker centroiding performance in dynamic imaging conditions," *2015 IEEE Aerospace Conference*, 2015, pp. 1–8, DOI: 10.1109/AERO.2015.7119226.

[10] X. Jiang, S. Li, L. Gu, J. Sun, and D. Xiao, "Optical Image Generation and High-precision Line-of-Sight Extraction for Mars Approach Navigation," *Journal of Navigation*, Vol. 72, No. 1, 2019, p. 229–252, DOI: 10.1017/S0373463318000450.

[11] M. Samaan and S. Theil, "Development of a low cost star tracker for the SHEFEX mission," *Aerospace Science and Technology*, Vol. 23, No. 1, 2012, pp. 469–478, DOI: 10.1016/j.ast.2011.09.013.

[12] A. Vyas, M. B. Roopashree, B. R. Prasad, and A. Vyas, "Performance of Centroiding Algorithms at Low Light Level Conditions in Adaptive Optics," *2009 International Conference on Advances in Recent Technologies in Communication and Computing*, 2009, pp. 366–369, DOI: 10.1109/ARTCom.2009.30.

[13] B. B. Spratling and D. Mortari, "A Survey on Star Identification Algorithms," *Algorithms*, Vol. 2, No. 1, 2009, pp. 93–107, DOI: 10.3390/a2010093.

[14] L. Markley and J. Crassidis, *Fundamentals of Spacecraft Attitude Determination and Control*. Springer-Verlag New York, 01 2014, DOI: 10.1007/978-1-4939-0802-8.

[15] R. Karimi and D. Mortari, "Interplanetary Autonomous Navigation Using Visible Planets," *Journal of Guidance, Control, and Dynamics*, Vol. 38, 04 2015, pp. 1–6, DOI: 10.2514/1.G000575.

[16] V. Franzese, *Autonomous Navigation for Interplanetary CubeSats at different scales*. PhD thesis, Politecnico di Milano, 2021.

[17] C. C. Liebe, "Accuracy performance of star trackers - a tutorial," *IEEE Transactions on Aerospace and Electronic Systems*, Vol. 38, April 2002, pp. 587–599, DOI: 10.1109/TAES.2002.1008988.

[18] M. A. C. Perryman, L. Lindegren, J. Kovalevsky, E. Hog, U. Bastian, P. L. Bernacca, M. Creze, F. Donati, M. Grenon, M. Grewing, F. van Leeuwen, H. van der Marel, F. Mignard, C. A. Murray, R. S. Le Poole, H. Schrijver, C. Turon, F. Arenou, M. Froeschle, and C. S. Petersen, "The Hipparcos Catalogue.," *Astronomy and Astrophysics*, Vol. 500, jul 1997, pp. 501–504.

[19] Y. Ma, S. Soatto, J. Kosecka, and S. S. Sastry, *An Invitation to 3-D Vision: From Images to Geometric Models*. SpringerVerlag, 2003.

[20] S. Du, M. Wang, X. Chen, S. Fang, and H. Su, "A High-accuracy Extraction Algorithm of Planet Centroid Image in Deep-space Autonomous Optical Navigation," *Journal of Navigation*, Vol. 69, No. 4, 2016, p. 828–844, 10.1017/S0373463315000910.

[21] M. Marin and H. Bang, "Design and Simulation of a High-Speed Star Tracker for Direct Optical Feedback Control in ADCS," *Sensors*, Vol. 20, Apr 2020, p. 2388, DOI: 10.3390/s20082388.

[22] P. K. Seidelmann, *Explanatory supplement to the astronomical almanac*. University Science Books, 2006.

[23] G. C. Holst, *CCD Arrays, Cameras and Displays*. SPIE-International Society for Optical Engine, 2 sub ed., 1998.

[24] W. Ogiers, K. Ruythooren, K. Wichelen, M. Dendoncker, S. Kowaltschek, and B. Razgus, "FAINTSTAR: an intelligent single-chip sensor head for star trackers—prototype results," *CEAS Space Journal*, Vol. 10, 09 2018, DOI: 10.1007/s12567-018-0220-x.

[25] T. Delabie, T. Durt, and J. Vandersteen, "Highly Robust Lost-in-Space Algorithm Based on the Shortest Distance Transform," *Journal of Guidance, Control, and Dynamics*, Vol. 36, No. 2, 2013, pp. 476–484, DOI: 10.2514/1.56860.